Journal of Biomedical Optics

SPIEDigitalLibrary.org/jbo

Assessment of human burn scars with optical coherence tomography by imaging the attenuation coefficient of tissue after vascular masking

Peijun Gong
Robert A. McLaughlin
Yih Miin Liew
Peter R. T. Munro
Fiona M. Wood
David D. Sampson

SPIE

Assessment of human burn scars with optical coherence tomography by imaging the attenuation coefficient of tissue after vascular masking

Peijun Gong,[a] Robert A. McLaughlin,[a] Yih Miin Liew,[b*] Peter R. T. Munro,[a,c] Fiona M. Wood,[d,e] and David D. Sampson[a,c]

[a]The University of Western Australia, School of Electrical, Electronic and Computer Engineering, Optical + Biomedical Engineering Laboratory, 35 Stirling Highway, Crawley, Western Australia 6009, Australia
[b]University of Malaya, Department of Biomedical Engineering, Faculty of Engineering, Kuala Lumpur 50603, Malaysia
[c]The University of Western Australia, Centre for Microscopy, Characterisation and Analysis, 35 Stirling Highway, Crawley, Western Australia 6009, Australia
[d]Royal Perth Hospital, Burns Service of Western Australia, Wellington Street, Perth, Western Australia 6000, Australia
[e]The University of Western Australia, School of Surgery, Burn Injury Research Unit, 35 Stirling Highway, Crawley, Western Australia 6009, Australia

Abstract. The formation of burn-scar tissue in human skin profoundly alters, among other things, the structure of the dermis. We present a method to characterize dermal scar tissue by the measurement of the near-infrared attenuation coefficient using optical coherence tomography (OCT). To generate accurate *en face* parametric images of attenuation, we found it critical to first identify (using speckle decorrelation) and mask the tissue vasculature from the three-dimensional OCT data. The resulting attenuation coefficients in the vasculature-masked regions of the dermis of human burn-scar patients are lower in hypertrophic (3.8 ± 0.4 mm^{-1}) and normotrophic (4.2 ± 0.9 mm^{-1}) scars than in contralateral or adjacent normal skin (6.3 ± 0.5 mm^{-1}). Our results suggest that the attenuation coefficient of vasculature-masked tissue could be used as an objective means to assess human burn scars. [DOI: 10.1117/1.JBO.19.2.021111]

Keywords: optical coherence tomography; parametric imaging; burn scars; hypertrophic scars; attenuation coefficient; scar assessment; collagen; vasculature.

Paper 130448SSR received Jun. 28, 2013; revised manuscript received Sep. 19, 2013; accepted for publication Sep. 20, 2013; published online Nov. 5, 2013.

1 Introduction

Wound healing after burn injury involves the sequential phases of inflammation, tissue formation, and tissue remodeling.[1] Scar formation during this process is a natural facet of healing, and hypertrophic scars are one pathology arising from an excessive response to injury during healing.[2] Such scars are characterized by prolific neovascularization; and excessive content[3–5] and abnormal arrangement of collagen.[6] In normal skin, collagen is arranged in a "basket-weave"-like structure, whereas collagen in hypertrophic scars is more unidirectionally aligned.[6,7] Previous studies have shown that, compared with normal skin, hypertrophic scars contain collagen fibrils with reduced diameter[6,8] and have higher water content.[9,10]

Various techniques are available or under investigation for the treatment of pathological scars including surgery, pressure therapy, corticosteroid injections, silicone gel sheeting, radiotherapy, and laser therapy.[11] Evaluating the efficacy of these clinical treatments typically requires the longitudinal assessment of a scar's severity. Current scar assessment methods are primarily based on the direct observation and palpation of the features of scars. For example, the Vancouver Scar Scale uses observer assessment of pigmentation, vascularity, pliability, and height to characterize the scar.[12] Assessment with such methods is inevitably somewhat subjective, leading to high inter-observer variability. There is reported research on alternative, less subjective techniques. Electron microscopy has been used to study the characteristic morphological profiles of pathological scars but requires histological slices of excised scar tissue.[6,13] Multiphoton[14,15] and confocal microscopies[16] have been applied to scar tissue or wounds, *ex vivo* and *in vivo*, including for high-resolution imaging of collagen and elastic fiber components. Ultrasound imaging has been investigated as a means of assessing the thickness of burn scars in pediatric patients noninvasively.[17] Other techniques, such as laser Doppler perfusion imaging and laser speckle perfusion imaging, have used the degree of vascularization as a surrogate indicator of scar status.[18]

Changes in tissue morphology in pathological scarring can result in changes in the optical properties of the tissue in the near-infrared wavelength range. This has driven a growing body of work exploring the use of optical coherence tomography (OCT) in scar assessment.[19–26] OCT is a noninvasive imaging modality capable of acquiring three-dimensional (3-D) scans of tissue at resolutions from 1 to 20 μm from superficial tissues at depths of up to 1 to 2 mm.[19] The morphological features of normal and diseased skin have been studied *in vivo* with OCT imaging.[20,21] Wound healing has been evaluated noninvasively by high-resolution OCT,[22] and polarization-sensitive (PS) OCT has been used to measure the birefringence of both normal and

*This author was with the Optical + Biomedical Engineering Laboratory, The University of Western Australia, when the majority of her contribution was made.

Address all correspondence to: Peijun Gong, The University of Western Australia, School of Electrical, Electronic and Computer Engineering, Optical + Biomedical Engineering Laboratory, 35 Stirling Highway, Crawley, Western Australia 6009, Australia. Tel: +61 8 6488 2317; Fax: +61 8 6488 1319; E-mail: gongp01@student.uwa.edu.au

0091-3286/2014/$25.00 © 2014 SPIE

burn-damaged human skin.[23,24] OCT has also been used to noninvasively assess vascularity as a measure of normal skin and scar status.[25,26]

For objective scar assessment, absolute quantities that characterize the tissue are required to monitor the progression of healing. One such quantity that may be extracted from OCT scans is the attenuation rate (parameterized by the attenuation coefficient), which is the rate at which the OCT signal decreases with depth in the tissue. This rate can be extracted by fitting the measured OCT signal versus depth (an A-scan) to a specific model.[27–29] Previous studies have shown that the attenuation coefficient measured with OCT can be used to distinguish between different types of tissue.[30–33] Previous research has also explored the attenuation coefficient of normal human skin tissue.[27,34,35] A very effective means of visualizing attenuation coefficients is through the presentation of *en face* maps, i.e., parametric images of the attenuation coefficient.[30,31] We hypothesize that differences in tissue microstructure between scarred and normal skin give rise to differences in the attenuation coefficient of near-infrared light. In this article, we extend the measurement of OCT attenuation coefficients and their presentation in parametric images to the case of pathological scarred tissue.

A difficulty arises when applying the attenuation coefficient method to *in vivo* OCT scans of skin. The vasculature of scarred and normal skin generates strong forward scattering at near-infrared wavelengths due, in part, to the high anisotropy and high scattering cross-section of red blood cells,[36] causing artificially high attenuation of the OCT signal that is not representative of the surrounding nonvascular component of the tissue. Here, we present an algorithm that automatically removes areas of vasculature from the calculations, allowing more accurate quantification of the attenuation coefficient of scarred and normal skin tissue. We present results from six clinically assessed scars that demonstrate a systematically lower attenuation coefficient of scarred tissue as compared with normal skin tissue and propose a mechanism explaining this observation.

2 Materials and Methods

2.1 *OCT Imaging*

A polarization-sensitive swept-source OCT system (PSOCT-1300, Thorlabs, Newton, New Jersy) with a central wavelength of 1325 nm was utilized to perform the scanning on patients. The measured axial and transverse resolutions (full-width-at-half-maximum) of the system are, respectively, 17 μm (in air) and 16 μm. Light illuminated the skin through an objective lens with a working distance of 25 mm to deliver a scanning beam with a numerical aperture of 0.03 and a measured optical power of 3.2 mW to the skin.

The tissue-imaging setup has been described in detail previously.[26] Briefly, a 10×10 mm outline was drawn on the skin to guide the attachment of a metal fiducial marker, which had a central hole (3-mm diameter) for imaging. The marker was used as a guide to remove motion artifacts, as previously described.[37] An adjustable spacer between the OCT scanner and the skin was used to maintain a suitable distance from the objective lens of the OCT scanner to the skin surface. A layer of ultrasound gel was applied to reduce the refractive index mismatch at the skin surface, thereby reducing imaging artifacts and enhancing the imaging depth.[38] The scanner was positioned on the skin and handheld during data acquisition.

Scans were acquired on six patients (age: 19 to 58 years, three females, three males) undergoing follow-up examination 12 or 24 months after initial treatment for burns. The scanning protocol was approved by the Human Research Ethics Committee of Royal Perth Hospital and The University of Western Australia. Written consent was obtained from all patients prior to scanning. For each patient, locations on the scar and on the contralateral or adjacent normal skin region were selected for 3-D OCT imaging. Each OCT data volume covered a region of $4 \times 1.5 \times 3$ mm ($1088 \times 1088 \times 512$ pixels) in the x, y (lateral), and z (axial into the skin) directions, respectively, acquired within the center of the outlined region, including a portion of the fiducial marker to enable motion correction. With these scanning parameters, over-sampling was used in order to record the speckle decorrelation for vasculature segmentation. The system was operated at an A-scan rate of ~4.9 kHz, leading to a B-scan rate of 4.5 frames per second and 3-D data volume acquisition time of ~4 min.

2.2 *Vasculature Masking*

The flow chart for vasculature masking is shown in the left column of Fig. 1. We denote by i^2 the sum of the squared OCT signals from the two detection channels of the PS-OCT system. This is equivalent to the square of a conventional OCT signal and is sometimes also referred to as the OCT signal power. In the remainder of this article, the term OCT data refers to i^2. Blood vessels were automatically segmented from this OCT data using speckle decorrelation.[39] In brief, the correlation between OCT data within a small moving window was calculated between pairs of adjacent B-scans, A and B, using the standard normalized cross-correlation equation:

$$\mathrm{corrMap}(x,z) = \frac{\sum_{p=1}^{M}\sum_{q=1}^{N}\{[i_A^2(x+p,z+q)-\overline{i_A^2(x,z)}][i_B^2(x+p,z+q)-\overline{i_B^2(x,z)}]\}}{\sqrt{\sum_{p=1}^{M}\sum_{q=1}^{N}[i_A^2(x+p,z+q)-\overline{i_A^2(x,z)}]^2}\sqrt{\sum_{p=1}^{M}\sum_{q=1}^{N}[i_B^2(x+p,z+q)-\overline{i_B^2(x,z)}]^2}}, \quad (1)$$

where the window size is $M \times N$, and i_A^2 and i_B^2 are OCT data from a pair of neighboring subimages in adjacent B-scans in an OCT data volume that are defined by the window. $\overline{i_A^2}$ and $\overline{i_B^2}$ are, respectively, the mean values of i_A^2 and i_B^2.

Regions of low cross-correlation in the resulting correlation volume image were identified as blood vessels. Motion artifacts caused by patient movement during scanning were then removed from this correlation volume by the use of a registration algorithm utilizing the metal fiducial marker. Details of the motion correction are described elsewhere.[37] By identifying the voxel of the lowest correlation (i.e., the highest decorrelation) along each A-scan (z-direction) at depths in the skin with adequately high OCT signal-to-noise ratio, a two-dimensional (2-D) *en face* maximum intensity projection (MIP) image of the vasculature was produced, showing the (x, y) locations of blood vessels. Further details of the algorithm were

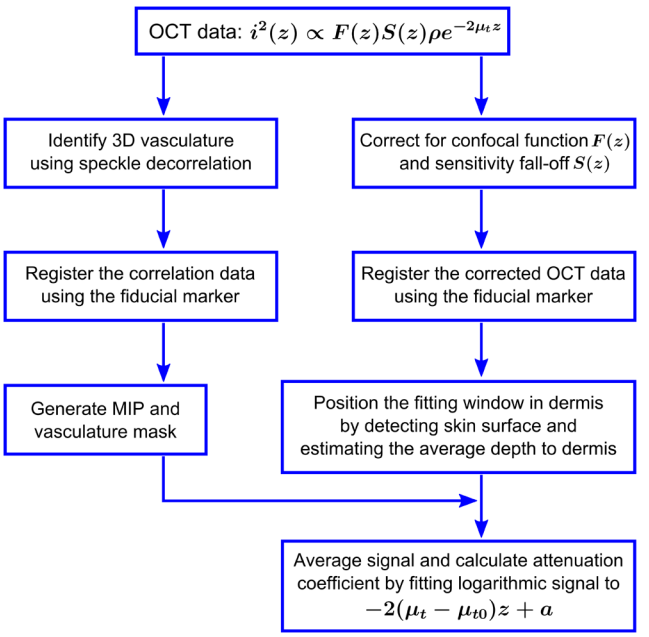

Fig. 1 Data processing flow for the calculation of the attenuation coefficient of vasculature-masked tissue in scarred and normal skin (see text for details). MIP: maximum intensity projection.

given previously.[26] This MIP image was then thresholded to form a binary mask of blood vessels, indicating (x, y) locations to be removed from subsequent calculation of the attenuation coefficient.

2.3 *Calculation of the Attenuation Coefficient*

Assuming that single scattering is the dominant scattering process, the rate of attenuation of the OCT signal with depth in a homogeneous sample follows a negative exponential function.[27] In addition, this signal is modulated by the confocal function of the focusing optics, and the sensitivity fall-off of our swept source OCT system. The skin OCT data, i^2, as a function of depth z can be expressed as follows:

$$i^2(z) \propto F(z)S(z)\rho e^{-2\mu_t z}, \tag{2}$$

where $F(z)$ and $S(z)$ are, respectively, the confocal and sensitivity fall-off functions, and $\rho e^{-2\mu_t z}$ represents the single-scattering component, where ρ is the initial value of the reflectance and μ_t is the attenuation coefficient.[31]

To extract the attenuation coefficient, we first corrected our *in vivo* scans for the confocal function and sensitivity fall-off of the system using a calibration scan of a low-scattering suspension of polystyrene microspheres (Polybead®, Polysciences, Inc., Warrington, Pennsylvania), as described by Scolaro et al.[31] The calibration OCT data can be written as

$$i_0^2(z) \propto F(z)S(z)\rho_0 e^{-2\mu_{t0} z}, \tag{3}$$

where ρ_0 is the initial value of the reflectance, and μ_{t0} is the attenuation coefficient of the calibration suspension. μ_{t0} was calculated to be 0.1 mm^{-1} at our OCT wavelength using Mie theory[40] and assuming negligible absorption. Each voxel value of the skin scans was corrected by division by the corresponding voxel value in the calibration scan volume. After taking the logarithm of the corrected data, the resulting logarithmic OCT data at each (x, y) location as a function of depth (z) is given by

$$\ln\left[\frac{i^2(z)}{i_0^2(z)}\right] = -2(\mu_t - \mu_{t0})z + a, \tag{4}$$

where a is a constant for each A-scan dependent on the ratio ρ/ρ_0.

The aforementioned fiducial marker-based registration algorithm was applied to the corrected OCT data to reduce the motion artifacts and to maintain the spatial consistency between the vasculature mask and the corrected OCT data. A Canny edge detector[41] was used to identify the surface of the skin. For each dataset, the average depth to the dermis from the tissue surface within the scan field-of-view was empirically estimated. Speckle was reduced using a moving window averaging function with a uniform kernel of 40×40 μm within the $x - y$ plane over regions not masked out. The attenuation coefficient μ_t was calculated from a linear least-squares fit to the averaged logarithmic OCT data over a depth of 200 μm from the average depth into the dermis [taking the refractive index of skin to be 1.43 (Ref. 42) to correct for the difference between physical and optical path length]. The goodness-of-fit of the least-squares regression was calculated to assess the fitting quality.

After performing the calculation on each A-scan at vasculature-masked locations covered by the central 1×1 mm $(x \times y)$ region, a 2-D image in the $x - y$ plane was generated with the attenuation coefficient represented graphically as the pixel intensity for each location. In addition, a one-dimensional normalized histogram was computed, comprising all attenuation values in the image (not including locations masked by the vasculature). Each histogram contained typically 100,000 to 170,000 values, corresponding to the number of vasculature-free A-scans in each dataset. The histogram shows the distribution of attenuation coefficients for scar tissue and the contralateral or adjacent normal skin tissue. All data processing was performed using MATLAB® (vR2012a, The MathWorks, Inc., Natick, Massachusetts).

3 Results

3.1 *Vasculature-Induced Artifacts*

Figure 2 shows the calculated attenuation coefficient and related data for normal skin on the lower right leg of a 19-year-old Caucasian male patient. The OCT scanning area (4×1.5 mm) was in the center of the region marked with a square outline (10×10 mm) on the skin, as shown in Fig. 2(a). Figure 2(b) shows the 2-D *en face* vasculature MIP of the scanning region. The blue square (1×1 mm) delineates the region over which the attenuation coefficient map in Fig. 2(c) was extracted using the corrected, registered, and averaged structural OCT data. The attenuation coefficient determined for all (vascular and nonvascular) tissue regions is shown. The corresponding goodness-of-fit ($0 \rightarrow$ poor fitting, $1 \rightarrow$ good fitting) is presented in Fig. 2(d). By comparing Figs. 2(b) and 2(c), it is apparent that the attenuation coefficient values in the circled vascular regions are much lower than in the surrounding tissues, even giving rise to nonphysical negative values. Figure 2(e) compares the normalized attenuation coefficient distribution between the vascular (i.e., blood vessels) and nonvascular (i.e., all tissue excepting blood vessels) regions and highlights

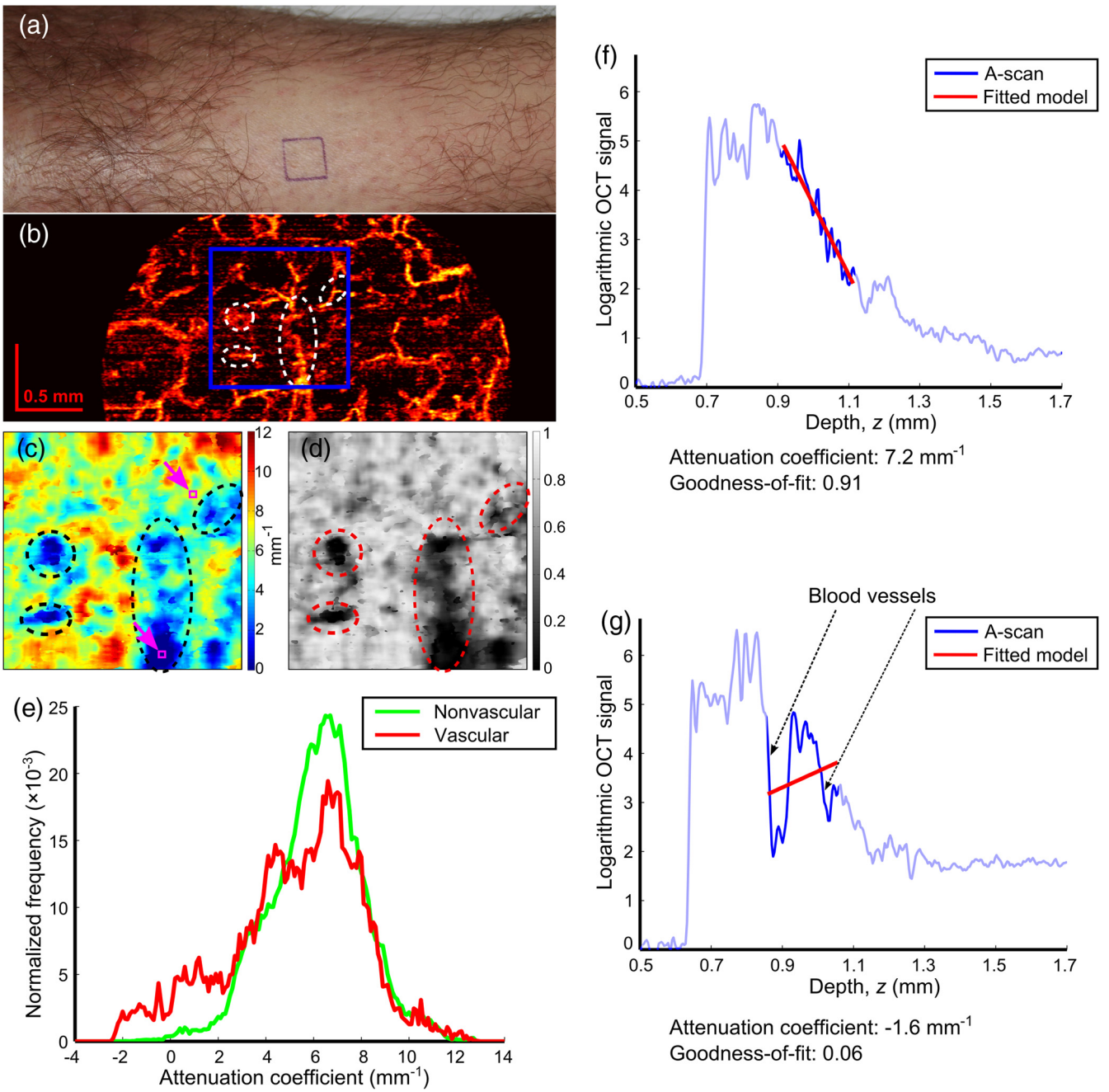

Fig. 2 Attenuation coefficient of normal skin showing the corrupting effect of the vasculature: (a) Photograph and (b) vasculature MIP of normal skin. (c, d) *En face* attenuation coefficient map and corresponding goodness-of-fit of the vascular and nonvascular tissues in the region outlined in blue in (b) (each image 1 × 1 mm). Examples of vascular regions are circled by the dotted lines in (b), (c), and (d). (e) Comparison of normalized attenuation coefficient distribution between vascular and nonvascular tissue regions. (f, g) Fitting examples, respectively, from nonvascular and vascular regions marked by the small purple squares and indicated by arrows in (c).

this problem. The attenuation coefficient distribution in the vascular region is artificially broadened and extended to low values.

Figures 2(f) and 2(g) show two representative fitting examples, respectively, for nonvascular and vascular tissues, marked by the two small purple squares in Fig. 2(c). The region of OCT signal used for the fitting (200 μm in length) is shown in blue, while the remainder of the A-scan is rendered partially transparent. The attenuation coefficient is extracted from the line of best fit (red) for each A-scan. Figure 2(f) demonstrates the applicability of the single-scattering model to the nonvascular dermal tissue with a high goodness-of-fit value of 0.91. In Fig. 2(g), the presence of two blood vessels at different depths gives rise to the sharp drops in the observed signal. The subsequent increase in the measured OCT signal below the first blood vessel gives rise to an apparent negative attenuation coefficient value with a poor goodness-of-fit value of 0.06. It is also evident from Fig. 2(d) that the low attenuation in the outlined vascular regions is accompanied by poor goodness-of-fit to the single-scattering, log-linear model. Since scarred skin has been shown to have larger blood vessel diameters and higher vasculature density than normal skin,[26] this vascular artifact is expected to be still more prominent in scar tissue. Consequently, we

incorporated a vasculature-masking step in the determination of the attenuation coefficient in order to minimize this corrupting effect.

3.2 *Case Study of a Hypertrophic Scar*

Figure 3 shows a 12-month-old hypertrophic scar originating from a hot water burn on the medial left inner forearm of a 30-year-old Caucasian female patient. Figures 3(a) and 3(b) are photographs of the contralateral normal skin and scar tissue, respectively. OCT scans were performed in the central 4×1.5 mm of the outlined regions. Figures 3(c) and 3(d) show the vasculature MIPs for the normal skin and scar, respectively, with the central blue squares (1×1 mm) identifying the regions for attenuation coefficient calculation. As noted by Liew et al.,[26] the vasculature is observed to be much more prolific in

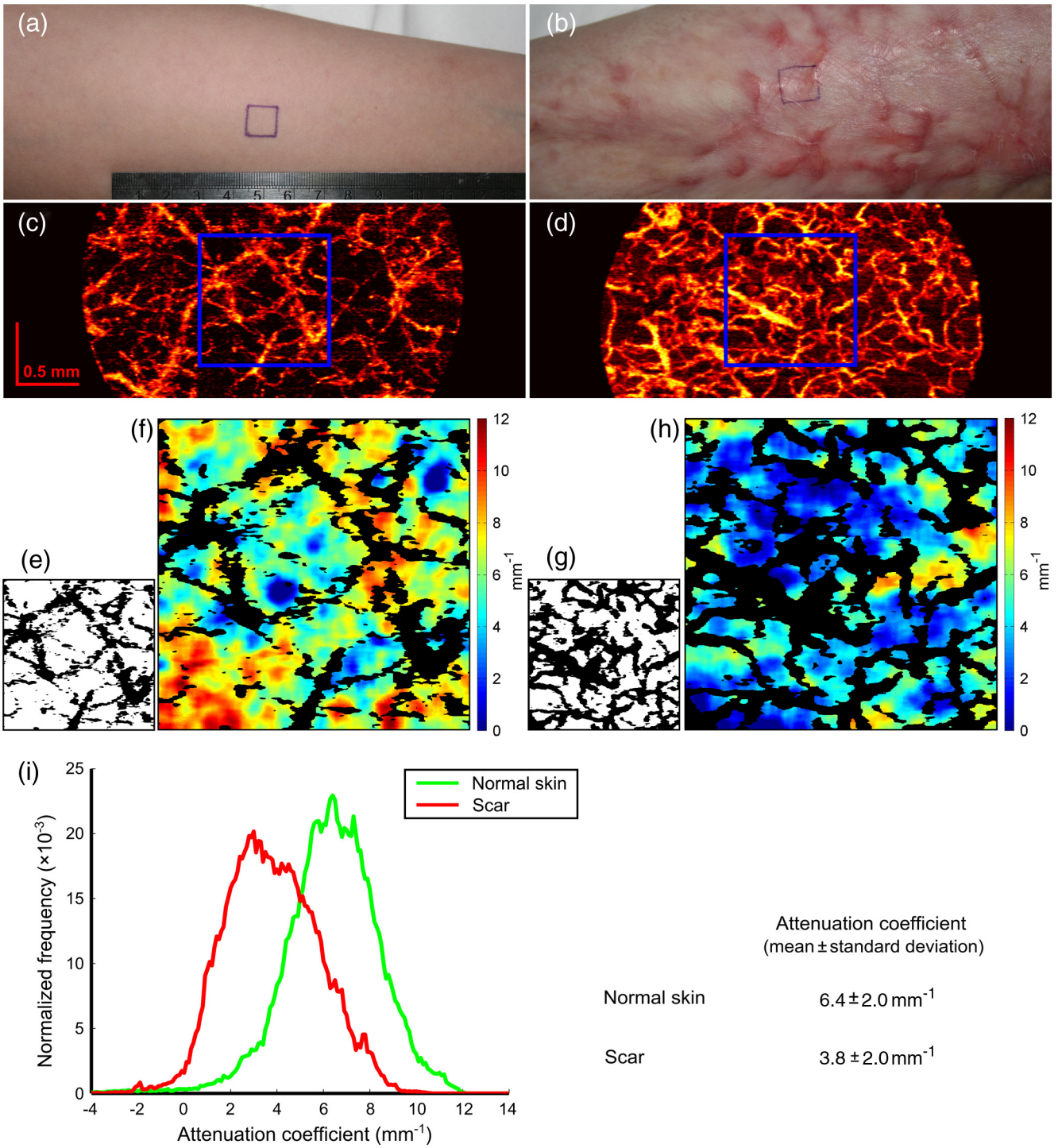

Fig. 3 Case study of the attenuation coefficient of a hypertrophic scar: (a, b) Photographs of the contralateral normal skin and scar. (c, d) Vasculature MIPs of the normal skin and scar in (a) and (b), respectively. (e, g) Vasculature masks for normal skin and scar (1×1 mm), respectively. (f, h) *En face* attenuation coefficient (mm^{-1}) maps of, respectively, normal skin and scar (1×1 mm). (i) Histogram of attenuation coefficients for normal skin and scar.

the scar tissue. Figures 3(e) and 3(g) depict the masks generated (black: vascular region; white: nonvascular region) after thresholding the vasculature MIPs. Figures 3(f) and 3(h) present the 2-D *en face* attenuation coefficient maps, respectively, for normal skin and scar. The attenuation coefficient is visibly lower in the hypertrophic scar than in the contralateral normal skin. From the distribution of attenuation coefficient values for each scan plotted in Fig. 3(i), we observe that the attenuation coefficients in scar tissue have a distribution of similar width to normal skin tissue but are on average much lower, with the mean attenuation coefficients of scar and normal skin being 3.8 and 6.4 mm^{-1}, respectively.

3.3 *Case Study of a Normotrophic Scar*

The results of a case study on a 12-month-old normotrophic scar are shown in Fig. 4. The scar, outlined in red in Fig. 4(a), was caused by a wood fire burn on the left lateral forearm of a 58-year-old Caucasian female. Figures 4(b) and 4(c) show MIPs of the vasculature of the contralateral normal skin (photograph not shown) and the scar, respectively. After masking of the vasculature using Figs. 4(d) and 4(f), the calculated attenuation coefficient maps are shown in Figs. 4(e) and 4(g). Figure 4(h) plots the normalized attenuation coefficient distribution of the scar and normal skin, which have mean values of 5.4 and 6.7 mm^{-1}, respectively. Note the increased degree of overlap of the distributions between this (nonpathological) normotrophic scar (red) and the contralateral normal skin (green), in comparison to the (pathological) hypertrophic scar in Fig. 3(i).

3.4 *Results from All Subjects*

The mean (±standard error) attenuation coefficient of the vasculature-masked dermal tissue in hypertrophic scars ($n = 3$), normotrophic scars ($n = 3$), and normal skin ($n = 6$), calculated from data on all subjects, is summarized in Fig. 5. The hypertrophic scars give rise to the lowest attenuation coefficient (3.8 ± 0.4 mm^{-1}); the normotrophic scars values are greater (4.2 ± 0.9 mm^{-1}); and the contralateral or adjacent normal skin has the largest values (6.3 ± 0.5 mm^{-1}). Student's *t*-test shows that the difference between the attenuation coefficients of the scar and normal skin is statistically significant ($p < 0.001$).

4 Discussion

In this study, we specifically focused on characterization of the dermis, since it undergoes very significant changes in content and structure during the wound healing process[2] and occupies most of the OCT imaging depth range. As the epidermis is only about 100-μm thick and is largely restored with new epidermal tissue during the wound healing process, we chose to exclude it. Our results show on average 36% lower dermal attenuation in scarred skin compared with normal skin. This strong effect can potentially be used as the basis for an objective method of scar characterization. As pathological scarring commonly leads to excessive production of both collagen fibers and blood vessels, the present method complements the scar assessment method solely based on vasculature that we have recently reported.[26] The integration of both methods could potentially be used to track the efficacy of various treatment strategies targeting both collagen fibers and blood vessels.

To explain the contrast that we observe in the vasculature-masked tissue, we have employed a model proposed by Jacques which has been shown to accurately describe the attenuation of light in the dermis.[43] This model was verified against measurements of the reduced scattering coefficient, $(1 - g)\mu_s$, where μ_s is the scattering coefficient and g is the anisotropy factor, of *ex vivo* samples of dermis.[44] Jacques' model treats scattering in the dermis as being equivalent to single scattering by a collection of infinite cylinders, each of which represents a collagen fiber. Jacques also considered the contribution of Rayleigh scattering by subwavelength scatterers, but it has been shown that Rayleigh scattering is insignificant compared with scattering by the collagen fibers at the wavelength of interest.[44] The key parameters in the model are, thus, the refractive index of the collagen fibers and the background material, the distribution of fiber diameters, and the volume fraction of collagen fibers. The refractive index of the collagen fibers was calculated by assuming that the fibers are composed of a combination of water and collagen. Mie theory, describing the scattering of light by infinite cylinders, was used to calculate μ_s and g.

In relating Jacques' model to the mathematical form of the OCT signal in Eq. (2), we note that μ_t is proportional to $\mu_s a(g)$, where $a(g)$ represents the directional nature of scattering.[45] We, however, found that g varies insignificantly compared with μ_s when contrasting normal skin and scarred tissue, enabling $a(g)$ to be neglected when assessing the relative magnitudes of μ_t for the normal and scar cases. We did not have access to data on the distribution of fiber diameters for the particular cases presented in this article. We, thus, approximate the two ensembles of fibers, i.e., scar and normal, by their mean diameter and spacing from the literature.[7,46] In particular, the mean spacing of collagen fibers has been found to be 10.37 μm and 8.53 μm for normal and scar tissues, respectively, while the mean diameter was found to be 5.39 and 5.77 μm, respectively. Thus, if all other parameters remained equal, the higher density of fibers would result in μ_s for scar tissue being larger than that for normal tissue. It has, however, been noted that the percentage of water content is greater in hypertrophic scar tissue than in normal tissue (approximately 64% in normal skin).[9,10] The water content of hypertrophic scar tissue has been found to vary with scar age and, in one study, varied monotonically between 85.1% for a 0.5-year-old scar to 63.8% for a 2-year-old scar.[9] Another study noted that the water content of hypertrophic scar was 82%, although the age of the scar was not noted.[10] We cannot suppose that this water content is identical to that likely to be found in the collagen fibers. We note, however, that Jacques[43] assumed a water content of 65% in his model, which is in agreement with the measured figure for normal skin tissue.

Our approach was, thus, to calculate the ratio $\mu_s^{\text{scar}}/\mu_s^{\text{normal}}$, where μ_s^{scar} and μ_s^{normal} are the scattering coefficients for scar and normal skin tissues, respectively, for different percentages of water content in scar collagen fibers, while the water content percentage of collagen fibers in normal skin was fixed at 64% consistent with the literature. We used refractive indices for water and collagen of 1.3241 and 1.4367 at a wavelength of 1325 nm, respectively.[47] The scattering coefficients were calculated using Mie theory for scattering by cylinders, at normal incidence, using the mathematical formulation presented by Bohren and Huffman.[40] Figure 6 shows the simulated ratio of scattering coefficient between scar and normal skin, $\mu_s^{\text{scar}}/\mu_s^{\text{normal}}$, as a function of water content in the scar collagen fibers. The green triangle and red circle highlight simulated scattering coefficient ratios between scar and normal skin of

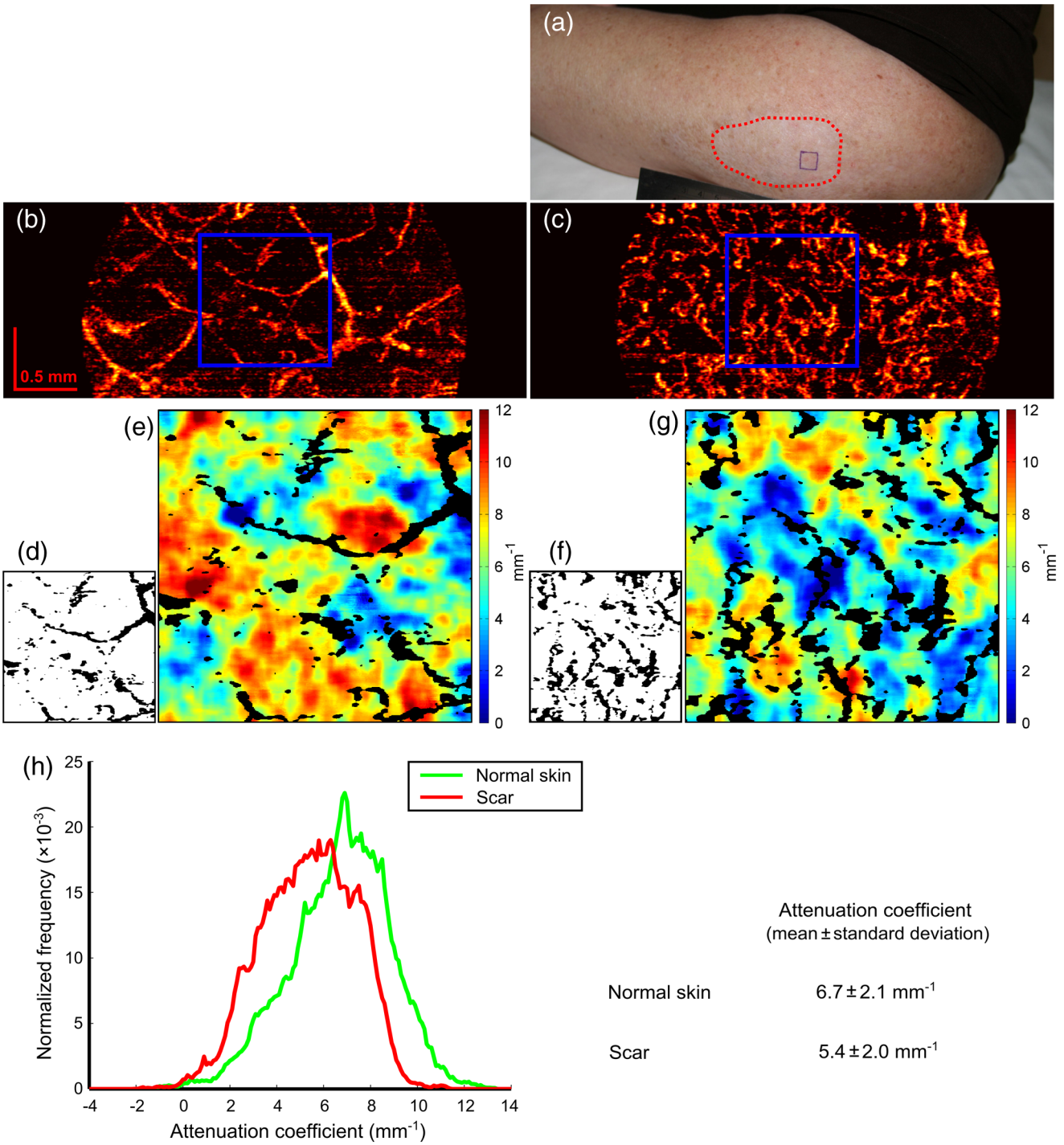

Fig. 4 Case study of the attenuation coefficient of a normotrophic scar. (a) Photograph of the scar (which is outlined in dotted red). (b, c) Vasculature MIPs of the normal skin and scar, respectively. (d, f) Vasculature masks for normal skin and scar (1 × 1 mm), respectively. (e, g) *En face* attenuation coefficient (mm^{-1}) maps of, respectively, normal skin and scar (1 × 1 mm). (h) Histogram of attenuation coefficients for normal skin and scar.

particular interest: respectively, for the water content percentage of 64% (2-year-old hypertrophic scars) and 85% (0.5-year-old hypertrophic scars).[9] The purple square corresponds to the ratio derived from our calculated attenuation coefficients of the scars and normal skin, and the resulting inferred water content (~76%) lies between that of the 0.5- and 2-year-old hypertrophic scars. This level is consistent with the 1.2-year-old mean age of the scars in this study but not with the lower reported water content of 1-year-old hypertrophic scars (66.5%).[9] Although requiring further study, our model and previous reports suggest that the contrast in attenuation coefficient may come from higher water content in scars. Thus, results of the type plotted in Fig. 6 could be used to study the water content in scar tissue noninvasively from measurement of the OCT attenuation coefficient ratio.

The masking of blood vessels removed a significant artifact from the calculation of the attenuation coefficient caused by the strong scattering by blood vessels. To the best of our knowledge,

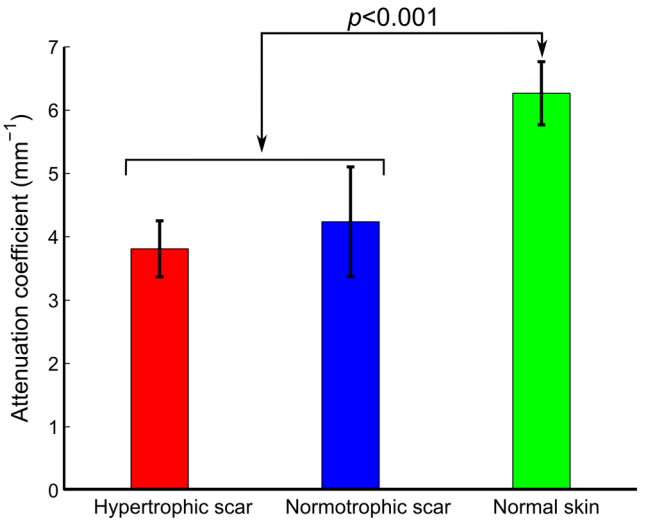

Fig. 5 Mean (±standard error) attenuation coefficient of hypertrophic scars ($n = 3$), normotrophic scars ($n = 3$), and normal skin ($n = 6$) of all subjects.

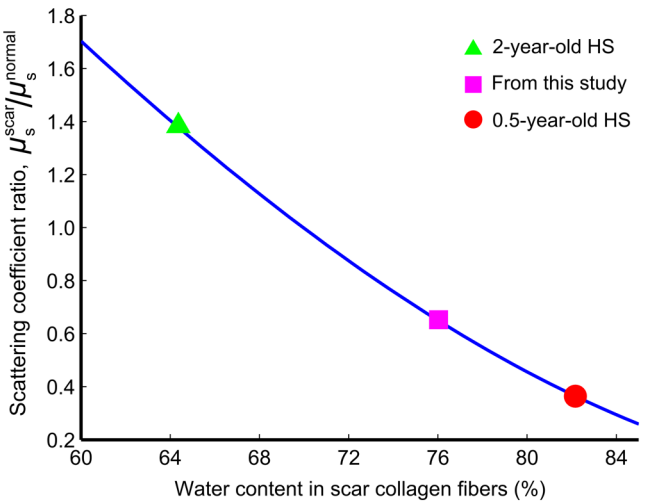

Fig. 6 Simulated $\mu_s^{scar}/\mu_s^{normal}$ ratios versus water content in scar collagen fibers. The triangle and circle represent water content values reported in the literature,[9] and the square represents the value calculated from the data in this study.

this is the first reported incorporation of vasculature masking into the calculation of attenuation coefficients from OCT data. Blood comprises plasma and other constituents, among which erythrocytes dominate the optical properties. Erythrocytes have a biconcave, disk-like shape with a size considerably larger than our OCT wavelength, which leads to strong forward scattering. This, together with the high-scattering cross-section and strong absorption of light,[36] generates a strong drop in the OCT signal, causing blood to exhibit a much higher attenuation coefficient than the nonvascular tissue in the skin. A previous study on fresh porcine blood, using 1300 nm OCT light, reported an attenuation coefficient of 12.15 mm^{-1},[48] which is almost twice the mean value of the vasculature-masked skin tissue measured in this study. This is particularly important in the evaluation of hypertrophic scars, which are known to have enhanced vasculature.[26] Analysis of the attenuation in these masked regions of blood flow may potentially provide additional information on metabolism such as the noninvasive monitoring of blood glucose concentration.[49]

Skin comprises a collection of microstructures with varying scattering and absorption properties. Quantification of scar and normal skin attenuation coefficients is complicated by tissue heterogeneity. Even after masking out the vasculature, heterogeneity in depth can invalidate the single-scattering exponential decay model and results in modified attenuation coefficient values, even negative values when the fitting window initiates in a low-signal region and extends into a high-signal region. We empirically found a fitting range of 200 μm in the dermis to be an appropriate compromise between including sufficient data in the estimate of the attenuation coefficient and minimizing the effects of tissue heterogeneity. The average attenuation coefficient of normal skin we determined using this fitting length is 6.3 ± 0.5 mm^{-1}, which lies between the results reported by Schmitt et al.[27] (4.6 to 4.7 mm^{-1}) and Kholodnykh et al.[34] (10 to 13 mm^{-1}) for forearm at 1300-nm wavelength. As discussed by Kholodnykh et al.,[34] the variation in attenuation coefficient could be caused by factors such as differences in experimental protocol, the use of a clearing agent, and variations in the skin tissue among individuals. One different feature of our experimental protocol from that of others is that we removed the contribution of blood vessels to target the nonvascular tissue.

In vivo OCT skin scanning can be affected by the motion between the scanner head and the skin. Such motion introduces image artifacts that distort the structural OCT images.[37] We used a fiducial marker fixed to the skin to guide a feature-based registration algorithm to remove such artifacts. However, motion artifacts also artificially increase speckle decorrelation, resulting in errors in blood vessel segmentation. An example of such an artifact appears as a pattern of horizontal lines in the vasculature MIP of Fig. 2(b). Alternative solutions have been proposed, such as rigidly affixing the scan head to the patient's skin,[50,51] although this can present additional difficulties when scanning acute burn wounds. Another feasible method is to reduce the 3-D data acquisition time, although this may reduce the sensitivity of vessel detection in areas of slow blood flow due to reduced speckle decorrelation between rapidly acquired B-scans.

5 Conclusions

In this article, we have presented a method for *in vivo* assessment of near-infrared attenuation coefficients of the dermis using OCT. We corrected for artifact caused by the presence of blood vessels using an automated method to segment and mask vasculature. We demonstrated the method of assessment on several *in vivo* human burn scars. Our results indicate that scars of mean age 1.2 years have on average 36% lower attenuation coefficients than contralateral or adjacent normal skin, and our modeling suggests that the lower attenuation coefficients arise from the previously reported increased water content in scars. This method could potentially be integrated with an automated vascularity quantification method in an objective scar assessment protocol to characterize both the vasculature and the connective tissue in scars. Future work will involve the investigation of this objective assessment protocol for the longitudinal study of human burn scars.

Acknowledgments

The authors thank Loretta Scolaro, Lixin Chin, Blake R. Klyen, Rodney W. Kirk, Dirk Lorenser, and Xiaojie Yang for discussions regarding the attenuation coefficient calculation and OCT data processing. The authors also thank Sharon Rowe at the Telstra Burn Reconstruction and Rehabilitation Unit, Royal Perth Hospital, for help in patient management. P. Gong acknowledges a joint scholarship from The University of Western Australia and the China Scholarship Council. R. A. McLaughlin is supported by a fellowship from Cancer Council Western Australia. P. R. T. Munro is supported by a Discovery Early Career Research Award from the Australian Research Council (DE120101331). This study is partially supported by the National Breast Cancer Foundation, Australia. Y. M. Liew was supported by a SIRF and UIS scholarship from The University of Western Australia.

References

1. A. J. Singer and R. A. F. Clark, "Cutaneous wound healing," *N. Engl. J. Med.* **341**(10), 738–746 (1999).
2. D. T. Nguyen, D. P. Orgill, and G. F. Murphy, "The pathophysiologic basis for wound healing and cutaneous regeneration," Chapter 4 in *Biomaterials for Treating Skin Loss*, D. Orgill and C. Blanco, Eds., pp. 25–57, Woodhead Publishing Limited, Cambridge, England (2009).
3. M. B. Witte and A. Barbul, "General principles of wound healing," *Surg. Clin. North Am.* **77**(3), 509–528 (1997).
4. F. B. Niessen et al., "On the nature of hypertrophic scars and keloids: a review," *Plast. Reconstr. Surg.* **104**(5), 1435–1458 (1999).
5. T. L. Tuan and L. S. Nichter, "The molecular basis of keloid and hypertrophic scar formation," *Mol. Med. Today* **4**(1), 19–24 (1998).
6. H. A. Linares et al., "The histiotypic organization of the hypertrophic scar in humans," *J. Invest. Dermatol.* **59**(4), 323–331 (1972).
7. P. D. H. M. Verhaegen et al., "Differences in collagen architecture between keloid, hypertrophic scar, normotrophic scar, and normal skin: an objective histopathological analysis," *Wound Repair Regen.* **17**(5), 649–656 (2009).
8. K. J. Stewart, "A quantitative ultrastructural study of collagen fibrils in human skin, normal scars, and hypertrophic scars," *Clin. Anat.* **8**(5), 334–338 (1995).
9. M. Babu et al., "Differentiation of keloid and hypertrophic scar; correlation of the water proton relaxation times with the duration of the scar," *Physiol. Chem. Phys. Med. NMR* **25**(2), 113–120 (1993).
10. C. W. Kischer and M. R. Shetlar, "Collagen and mucopolysaccharides in the hypertrophic scar," *Connect. Tissue Res.* **2**(3), 205–213 (1974).
11. T. A. Mustoe et al., "International clinical recommendations on scar management," *Plast. Reconstr. Surg.* **110**(2), 560–571 (2002).
12. Z. Tyack et al., "A systematic review of the quality of burn scar rating scales for clinical and research use," *Burns* **38**(1), 6–18 (2012).
13. M. Santucci et al., "Keloids and hypertrophic scars of Caucasians show distinctive morphologic and immunophenotypic profiles," *Virchows Archiv* **438**(5), 457–463 (2001).
14. J. Chen et al., "Multiphoton microscopy study of the morphological and quantity changes of collagen and elastic fiber components in keloid disease," *J. Biomed. Opt.* **16**(5), 051305 (2011).
15. V. Da Costa et al., "Nondestructive imaging of live human keloid and facial tissue using multiphoton microscopy," *Arch. Facial Plast. Surg.* **10**(1), 38–43 (2008).
16. S. Lange-Asschenfeldt et al., "Applicability of confocal laser scanning microscopy for evaluation and monitoring of cutaneous wound healing," *J. Biomed. Opt.* **17**(7), 076016 (2012).
17. X. Q. Wang et al., "Ultrasound assessed thickness of burn scars in association with laser Doppler imaging determined depth of burns in paediatric patients," *Burns* **36**(8), 1254–1262 (2010).
18. C. J. Stewart et al., "A comparison of two laser-based methods for determination of burn scar perfusion: Laser Doppler versus laser speckle imaging," *Burns* **31**(6), 744–752 (2005).
19. W. Drexler and J. G. Fujimoto, *Optical Coherence Tomography: Technology and Applications*, Springer, Berlin (2008).
20. J. Welzel et al., "Optical coherence tomography of the human skin," *J. Am. Acad. Dermatol.* **37**(6), 958–963 (1997).
21. J. Welzel, "Optical coherence tomography in dermatology: a review," *Skin Res. Technol.* **7**(1), 1–9 (2001).
22. M. J. Cobb et al., "Noninvasive assessment of cutaneous wound healing using ultrahigh-resolution optical coherence tomography," *J. Biomed. Opt.* **11**(6), 064002 (2006).
23. M. C. Pierce et al., "Birefringence measurements in human skin using polarization-sensitive optical coherence tomography," *J. Biomed. Opt.* **9**(2), 287–291 (2004).
24. K. H. Kim et al., "*In vivo* imaging of human burn injuries with polarization-sensitive optical coherence tomography," *J. Biomed. Opt.* **17**(6), 066012 (2012).
25. F. Bazant-Hegemark et al., "Multi-beam resolution video-rate swept-source optical coherence tomography (OCT) provides endogenous contrast for in vivo blood flow independent of flow direction," *Proc. SPIE* **7554**, 75542Z (2010).
26. Y. M. Liew et al., "*In vivo* assessment of human burn scars through automated quantification of vascularity using optical coherence tomography," *J. Biomed. Opt.* **18**(6), 061213 (2013).
27. J. M. Schmitt, A. Knüttel, and R. F. Bonner, "Measurement of optical properties of biological tissues by low-coherence reflectometry," *Appl. Opt.* **32**(30), 6032–6042 (1993).
28. J. M. Schmitt and A. Knüttel, "Model of optical coherence tomography of heterogeneous tissue," *J. Opt. Soc. Am. A* **14**(6), 1231–1242 (1997).
29. L. Thrane, H. T. Yura, and P. E. Andersen, "Analysis of optical coherence tomography systems based on the extended Huygens-Fresnel principle," *J. Opt. Soc. Am. A* **17**(3), 484–490 (2000).
30. R. A. McLaughlin et al., "Parametric imaging of cancer with optical coherence tomography," *J. Biomed. Opt.* **15**(4), 046029 (2010).
31. L. Scolaro et al., "Parametric imaging of the local attenuation coefficient in human axillary lymph nodes assessed using optical coherence tomography," *Biomed. Opt. Express* **3**(2), 366–379 (2012).
32. C. Xu et al., "Characterization of atherosclerosis plaques by measuring both backscattering and attenuation coefficients in optical coherence tomography," *J. Biomed. Opt.* **13**(3), 034003 (2008).
33. F. J. van der Meer et al., "Localized measurement of optical attenuation coefficients of atherosclerotic plaque constituents by quantitative optical coherence tomography," *IEEE Trans. Med. Imaging* **24**(10), 1369–1376 (2005).
34. A. I. Kholodnykh et al., "Accurate measurement of total attenuation coefficient of thin tissue with optical coherence tomography," *IEEE J. Sel. Top. Quant. Electron.* **9**(2), 210–221 (2003).
35. P. Lee, W. Gao, and X. Zhang, "Performance of single-scattering model versus multiple-scattering model in the determination of optical properties of biological tissue with optical coherence tomography," *Appl. Opt.* **49**(18), 3538–3544 (2010).
36. A. Roggan et al., "Optical properties of circulating human blood in the wavelength range 400–2500 nm," *J. Biomed. Opt.* **4**(1), 36–46 (1999).
37. Y. M. Liew et al., "Motion correction of in vivo three-dimensional optical coherence tomography of human skin using a fiducial marker," *Biomed. Opt. Express* **3**(8), 1774–1786 (2012).
38. Y. M. Liew et al., "Reduction of image artifacts in three-dimensional optical coherence tomography of skin in vivo," *J. Biomed. Opt.* **16**(11), 116018 (2011).
39. J. Enfield, E. Jonathan, and M. Leahy, "*In vivo* imaging of the microcirculation of the volar forearm using correlation mapping optical coherence tomography (cmOCT)," *Biomed. Opt. Express* **2**(5), 1184–1193 (2011).
40. C. F. Bohren and D. R. Huffman, *Absorption and Scattering of Light by Small Particles*, Wiley, New York (1983).
41. J. Canny, "A computational approach to edge detection," *IEEE Trans. Pattern Anal. Mach. Intell.* **PAMI-8**(6), 679–698 (1986).
42. T. Gambichler et al., "*In vivo* data of epidermal thickness evaluated by optical coherence tomography: effects of age, gender, skin type, and anatomic site," *J. Dermatol. Sci.* **44**(3), 145–152 (2006).
43. S. L. Jacques, "Origins of tissue optical properties in the UVA, visible and NIR regions," in *OSA TOPS on Advances in Optical Imaging and Photon Migration*, R. R. Alfano and J. G. Fujimoto, Eds., Vol. 2, pp. 364–371, Optical Society of America, Washington, DC (1996).

44. I. S. Saidi, S. L. Jacques, and F. K. Tittel, "Mie and Rayleigh modeling of visible-light scattering in neonatal skin," *Appl. Opt.* **34**(31), 7410–7418 (1995).
45. D. Levitz et al., "Quantitative characterization of developing collagen gels using optical coherence tomography," *J. Biomed. Opt.* **15**(2), 026019 (2010).
46. P. D. Verhaegen et al., "Adaptation of the dermal collagen structure of human skin and scar tissue in response to stretch: an experimental study," *Wound Repair Regen.* **20**(5), 658–666 (2012).
47. A. N. Bashkatov et al., "Estimation of wavelength dependence of refractive index of collagen fibers of scleral tissue," *Proc. SPIE* **4162**, 265–268 (2000).
48. D. P. Popescu and M. G. Sowa, "*In vitro* assessment of optical properties of blood by applying the extended Huygens-Fresnel principle to time-domain optical coherence tomography signal at 1300 nm," *Int. J. Biomed. Imaging* **2008**, 591618 (2008).
49. R. O. Esenaliev et al., "Noninvasive monitoring of glucose concentration with optical coherence tomography," *Opt. Lett.* **26**(13), 992–994 (2001).
50. C. Blatter et al., "*In situ* structural and microangiographic assessment of human skin lesions with high-speed OCT," *Biomed. Opt. Express* **3**(10), 2636–2646 (2012).
51. K. König et al., "Clinical optical coherence tomography combined with multiphoton tomography of patients with skin diseases," *J. Biophotonics* **2**(6–7), 389–397 (2009).